Unveiling the electrolyte effects of CO2 electroreduction to CO and H2 evolution from the interfacial pH perspective

Liu, X.

Appendix A

Supporting Information to Chapter 2

Calculation of the interfacial disc pH

The relationship between the concentration of protons at the disk and at the ring is shown in Equation S1[1], originally derived by Albery and Calvo, and the extended theory taking the autoprotolysis of water into account in Equation S2 by Yokoyama et al.[2] (for unbuffered systems). Here, c_r and c_d are the concentrations of either H^+ or OH^- at the ring and disk, respectively. c_∞ is the electrolyte bulk proton concentration and N_D is the detection efficiency. N_D is given by Equation S3 and Equation S4 and calculated based on the electrode geometry (Figure S2). Figure S2a and Figure S2b show the theoretical relationship between the interfacial ring (pH_{ring}) and disc (pH_{disc}) pH for unbuffered solutions of different bulk pH using Equation S1 and Equation S2, respectively. Here, it becomes clear how the description from Yokoyama is more sensitive in a wider pH range (for a direct comparison see Figure 2 in Yokoyama et al.[2]).

$$c_r = c_\infty + N_D(c_d - c_\infty) \qquad \text{Equation S1}$$

$$c_{r,H^+} - c_{r,OH^-} = N_D\left(c_{d,H^+} - c_{d,OH^-}\right) + (1 - N_D)\left(c_{\infty,H^+} - c_{\infty,OH^-}\right) \qquad \text{Equation S2}$$

$$N_D = 1 - \frac{1}{6}F\left[\left(\frac{r_2}{r_1}\right)^3 - 1\right] - \frac{2}{3}F\left[\left(\frac{r_2+r_3}{2r_1}\right)^3 - 1\right] - \frac{1}{6}F\left[\left(\frac{r_3}{r_1}\right)^3 - 1\right] \qquad \text{Equation S3}$$

Where *F*[x] is:

$$F[x] = \frac{3^{\frac{1}{2}}}{4\pi}\ln\left(\frac{\left(1+x^{\frac{1}{3}}\right)^3}{1+x}\right) + \frac{3}{2}\tan^{-1}\left(\frac{2x^{\frac{1}{3}}-1}{3^{\frac{1}{2}}}\right) + \frac{1}{4} \qquad \text{Equation S4}$$

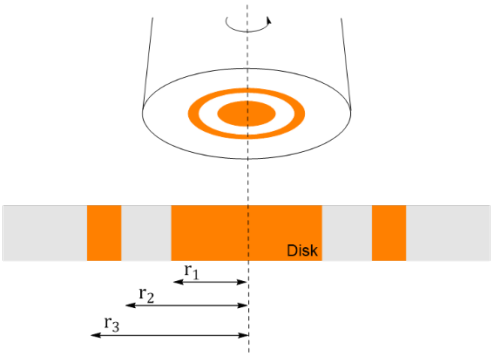

Figure S1. Schematic representation of the rotating ring-disc electrode with the geometrical parameters from Equation S3 indicated.

For buffered systems, we correct Equation S2 to take into account the homogeneous reaction taking place in solution, in the case of our work, involving the phosphate species in the electrolyte. In this case, the consumption of OH^- by the different phosphate species in considered and the corrected concentration of OH^- (c'_{OH^-}) is given by:

$c'_{OH^-} = c_{OH^-} + [H_2PO_4^-] + 2\ [HPO_4^{2-}] + 3\ [PO_4^{3-}]$ Equation S5

The following equilibrium constants and equations were used to calculate the concentration of phosphate species[3]:

$H_3PO_4 \rightleftharpoons H_2PO_4^- + H^+ \quad K_{a1} = 7.5 \times 10^{-3}$ Equation S6

$H_2PO_4^- \rightleftharpoons HPO_4^{2-} + H^+ \quad K_{a2} = 6.2 \times 10^{-8}$ Equation S7

$HPO_4^{2-} \rightleftharpoons PO_4^{3-} + H^+ K_{a3} = 2.14 \times 10^{-13}$ Equation S8

The total concentration of species is given by *TC* and the concentration of each species to be used in Equation S5 is determined based on Equations S9-S13:

$TC = [H_3PO_4] + [H_2PO_4^-] + [HPO_4^{2-}] + [PO_4^{3-}]$ Equation S9

$[H_3PO_4] = \frac{TC[H^+]^3}{[H^+]^3 + K_{a1}[H^+]^2 + K_{a1}K_{a2}[H^+] + K_{a1}K_{a2}K_{a3}}$ Equation S10

$[H_2PO_4^-] = \frac{TCK_{a1}[H^+]^2}{[H^+]^3 + K_{a1}[H^+]^2 + K_{a1}K_{a2}[H^+] + K_{a1}K_{a2}K_{a3}}$ Equation S11

$[HPO_4^{2-}] = \frac{TCK_{a1}K_{a2}[H^+]}{[H^+]^3 + K_{a1}[H^+]^2 + K_{a1}K_{a2}[H^+] + K_{a1}K_{a2}K_{a3}}$ Equation S12

$[PO_4^{3-}] = \frac{TCK_{a1}K_{a2}K_{a3}}{[H^+]^3 + K_{a1}[H^+]^2 + K_{a1}K_{a2}[H^+] + K_{a1}K_{a2}K_{a3}}$ Equation S13

Finally, expanding Equation S5, the relationship between the interfacial pH_{ring} and pH_{disc} for a phosphate buffered electrolyte is given by Equation S14.

$N_D = \frac{c_{r,OH^-} + [H_2PO_4^-]_r + 2\,[HPO_4^{2-}]_r + 3\,[PO_4^{3-}]_r - c_{\infty,OH^-} - [H_2PO_4^-]_\infty - 2\,[HPO_4^{2-}]_\infty - 3\,[PO_4^{3-}]_\infty}{c_{d,OH^-} + [H_2PO_4^-]_d + 2\,[HPO_4^{2-}]_d + 3\,[PO_4^{3-}]_d - c_{\infty,OH^-} - [H_2PO_4^-]_\infty - 2\,[HPO_4^{2-}]_\infty - 3\,[PO_4^{3-}]_\infty}$ Equation S14

A quartic equation can be derived from Equation S5-S14, where *a*, *b*, *c*, *d*, and *e* are parameters of C_{r,OH^-}, and *x* stands for C_{d,H^+}.

$ax^4 + bx^3 + cx^2 + dx + e = 0$ Equation S15

Solving the equation, four roots can be obtained and the nature of which can be inferred from the sign of the discriminants Δ, P and D. In our cases, all the roots are real and distinct roots since the Δ>0, P<0 and D<0.

$\Delta = 256a^3e^3 - 192a^2bde^2 - 128a^2c^2e^2 + 144a^2cd^2e - 27a^2d^4 + 144ab^2ce^2 - 6ab^2d^2e - 80abc^2de + 18abcd^3 + 16ac^4e - 4ac^3d^2 - 27b^4e^2 + 18b^3cde - 4b^3d^3 - 4b^2c^3e + b^2c^2d^2$ Equation S16

$P = 8ac - 3b^2$ Equation S17

$D = 64a^3e - 16a^2c^2 + 16ab^2c - 16a^2bd - 3b^4$ Equation S18

So that

$x_{1,2} = -\frac{b}{4a} - S \pm \frac{1}{2}\sqrt{-4S^2 - 2p + \frac{q}{S}}$ Equation S19

$$x_{3,4} = -\frac{b}{4a} + S \pm \frac{1}{2}\sqrt{-4S^2 - 2p - \frac{q}{S}}$$ Equation S20

Where:

$$p = \frac{8ac-3b^2}{8a^2}$$ Equation S21

$$q = \frac{b^3-4abc+8a^2d}{8a^3}$$ Equation S22

$$S = -\frac{1}{2}\sqrt{-\frac{2}{3}p + \frac{2}{3a}\sqrt{\Delta_0}\cos\frac{\varphi}{3}}$$ Equation S21

$$\varphi = \cos^{-1}\left(\frac{\Delta_1}{2\sqrt{\Delta_0^3}}\right)$$ Equation S22

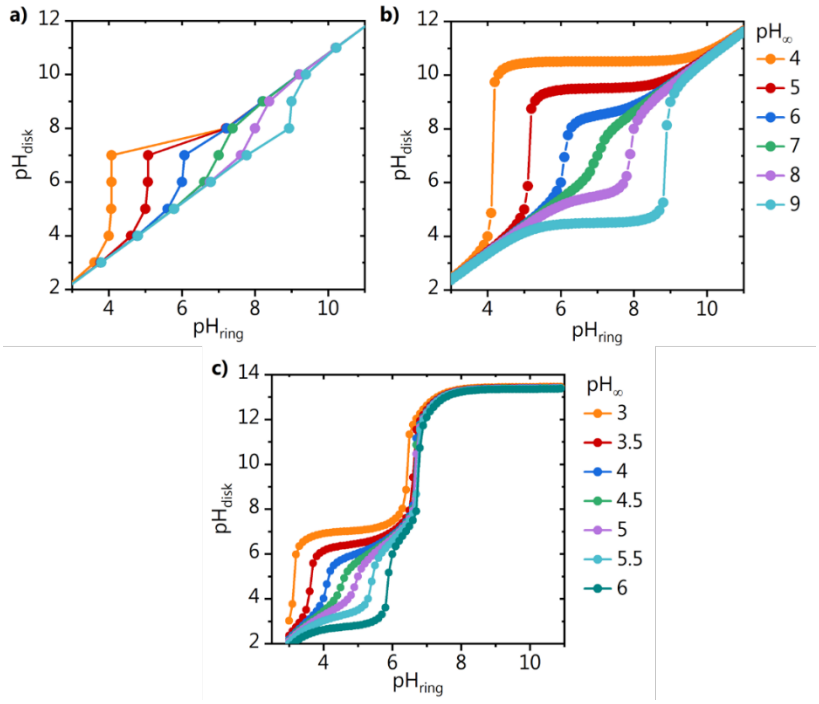

Figure S2. Theoretical relationship between interfacial pH_{ring} and pH_{disk} for different bulk pH (pH_∞) using a) the analytical equation reported by Albery and Calvo[1] and b) the extended theory, reported by Yokoyama et al.[2] (both for unbuffered systems), and c) the correction presented in this work for a phosphate buffered electrolyte.

With:

$\Delta_0 = c^2 - 3bd + 12ae$ Equation S23

$\Delta_1 = 2c^3 - 9bcd + 27b^2e + 27ad^2 - 72ace$ Equation S24

The analytical equations S19 and S20 are solved analytically. C_{d,H^+} can be determined out of the four solutions by limiting x (C_{d,H^+}) to be positive and relatively smaller than the corresponding C_{r,H^+}. The theoretical relationship that can be obtained using this description between the interfacial ring (pH_{ring}) and disc (pH_{disc}) pH for phosphate buffered solutions of different bulk pH is shown in Figure S2c.

pH measurements

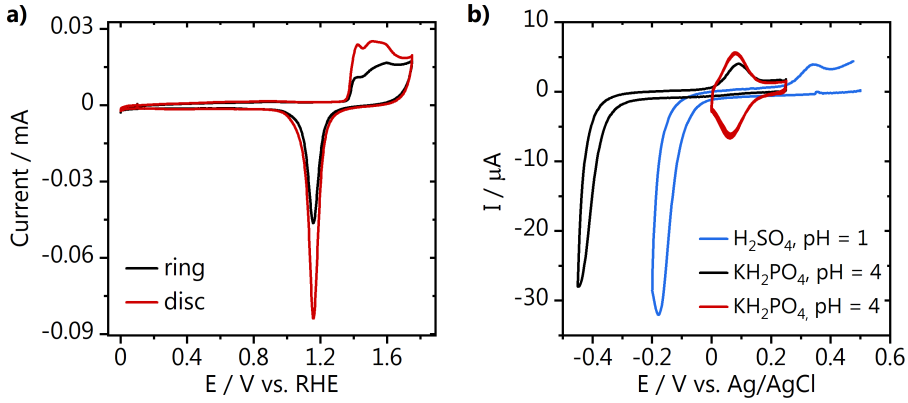

Figure S3. a) Blank voltammetry of the ring (black) and disc (red) electrodes taken in 0.1 M H_2SO_4 at 50 mV s^{-1}. b) cyclic voltammetry of the 4-NTP to 4-HATP conversion in 0.1 M KH_2PO_4 (black, 100 mV s^{-1}) and 0.1 M H_2SO_4 (blue), together with a characterization of the 4-HATP/4-NSTP redox couple (red, 200 mV s^{-1}) in phosphate.

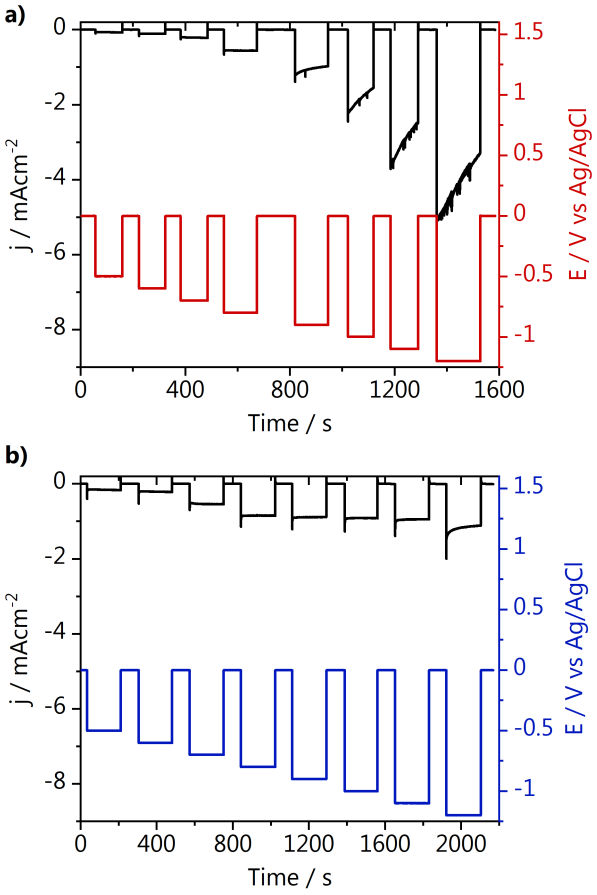

Figure S 4. Chronoamperometry from pH measurements at different potentials in 0.1 M argon saturated a) KH_2PO_4 pH_{bulk} = 4.4 and b) K_2SO_4 pH_{bulk} = 3.6 at 1600 rpm.

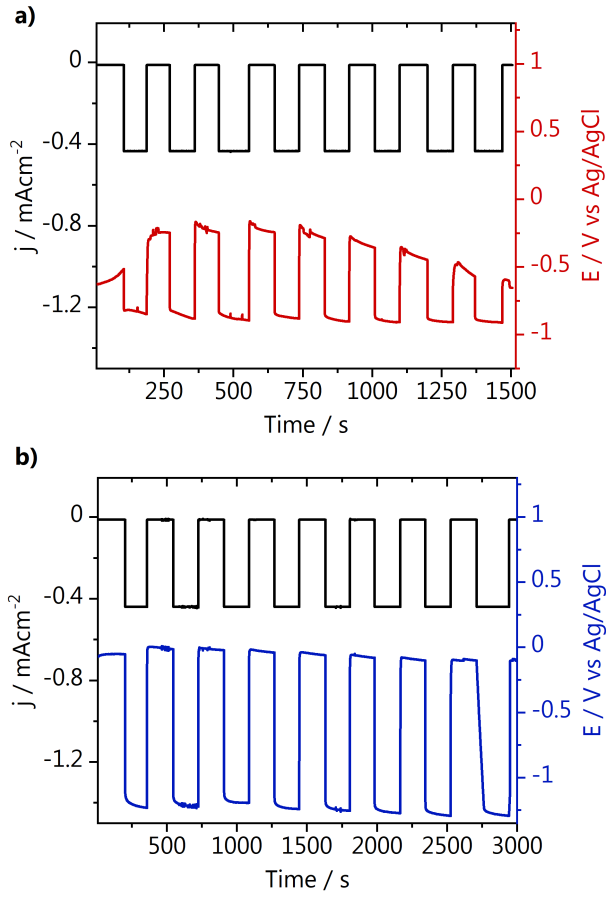

Figure S 5. Chronopotentiometry from pH measurements in 0.1 M argon saturated a) KH_2PO_4 pH_{bulk} = 4.4 and b) K_2SO_4 pH_{bulk} = 4.0 at different rotations (500, 750, 1000, 1250, 1500, 1750, 2000, 2600 rpm).

A

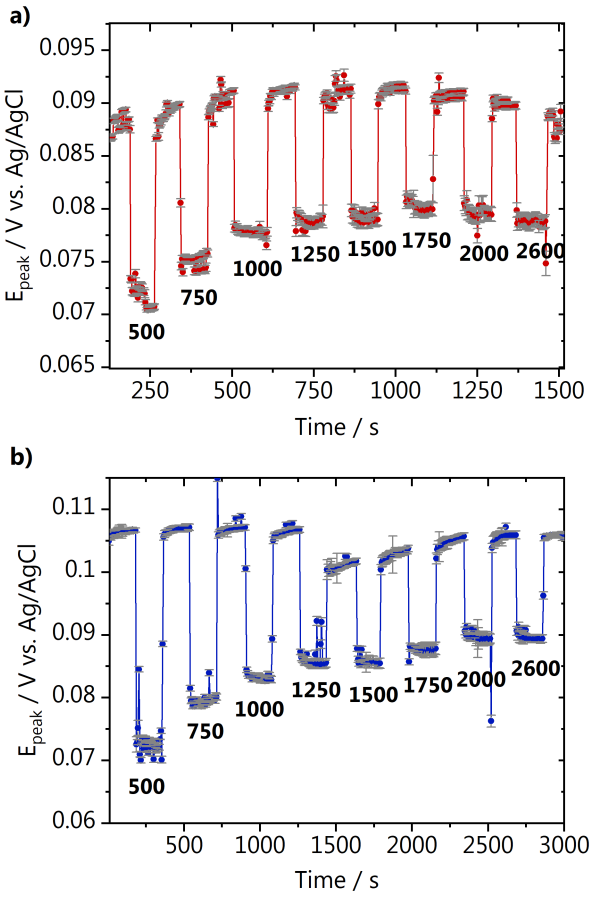

Figure S 6. Mid-peak potential extracted from the 4-HATP/4-NSTP voltammetry for the experiment in 0.1 M argon saturated a) KH_2PO_4 pH_{bulk} = 4.4 and b) K_2SO_4 pH_{bulk} = 4.0 at different rotations (500, 750, 1000, 1250, 1500, 1750, 2000, 2600 rpm).

References

[1] E. J. Calvo, W. J. Albery, *J. Chem. Soc. Faraday Trans. 1* **1983**, *79*, 2583–2596.

[2] Y. Yokoyama, K. Miyazaki, Y. Miyahara, T. Fukutsuka, T. Abe, *ChemElectroChem* **2019**, 4750–4756.

[3] K. J. Powell, P. L. Brown, R. H. Byrne, T. Gajda, G. Hefter, S. Sjöberg, H. Wanner, *Pure Appl. Chem.* **2005**, *77*, 739–800.

Appendix B

Supporting Information to Chapter 3

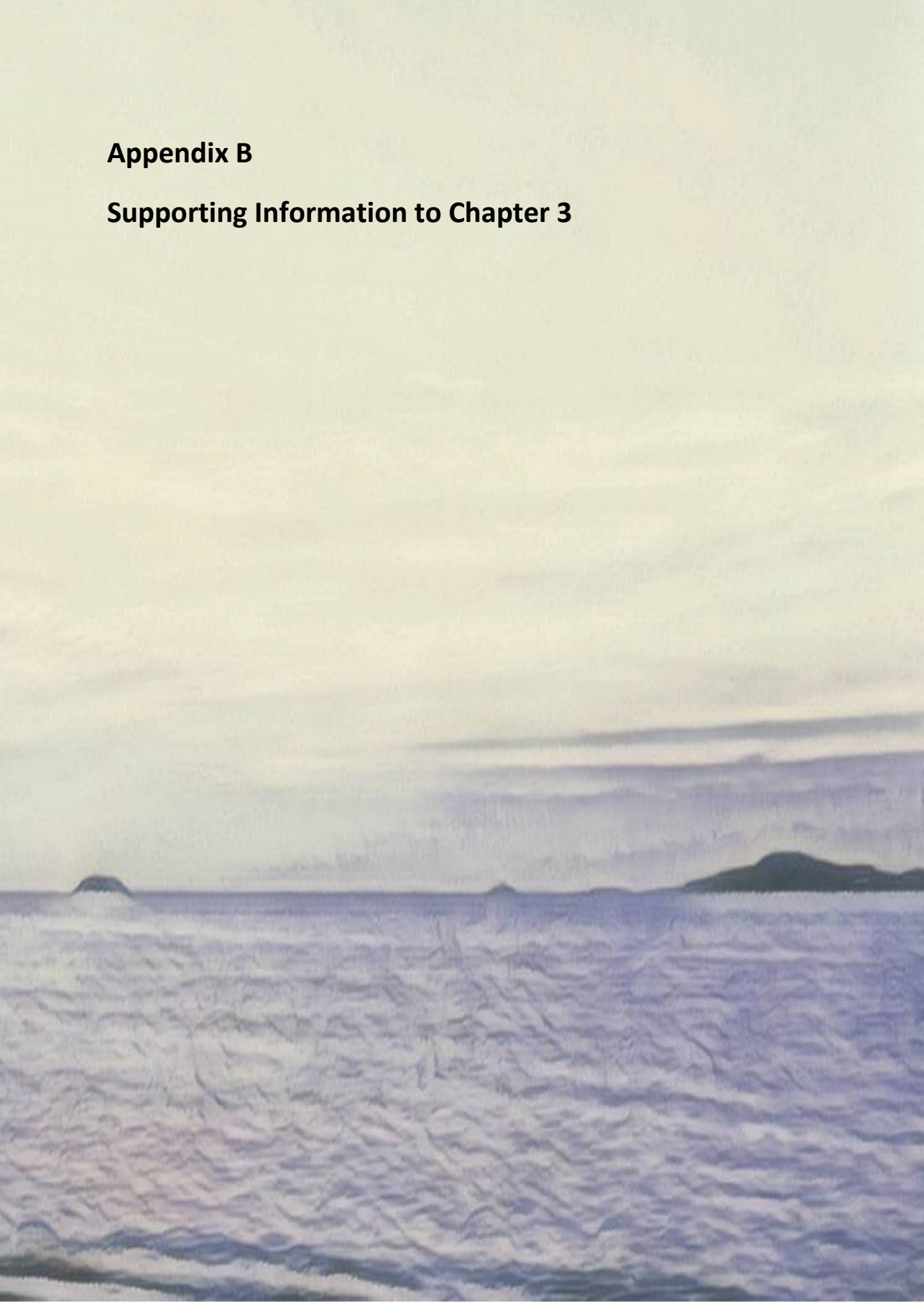

Cyclic voltammograms of 4-NTP reduction

As shown in Figure S1a, before measurements, to confirm the cleanliness of the electrodes and measure the ECSA, both ring and disk electrodes were characterized in Ar-saturated 0.1 M H_2SO_4 by cyclic voltammetry between 0 and 1.75 V vs RHE. After that, the gold ring was modified with the 4-NTP molecule, and then the 4-NTP was converted into the pH sensing redox couple 4-NSTP/4-HATP using a voltammetry in 0.1 M H_2SO_4 from 0.68 V vs RHE at 100 mV s^{-1} (Figure S1b). During the negative-going potential sweep, part of the 4-NTP is reduced completely to 4-ATP through a 6-proton-6-electron pathway, [1] while some 4-NTP was reduced partially to the 4-NSTP through a 4-proton-4-electron pathway, and the 4-NSTP is re-oxidized to 4-HATP in the positive-going potential sweep (Figure S1c). [2] As intermediates of the reduction, the content of 4-NSTP/4-HATP drops with decreasing lower vertex potentials (Figure S1d). Therefore, 0.11V vs RHE was used as lower vertex potential to optimize signals from the redox couple.

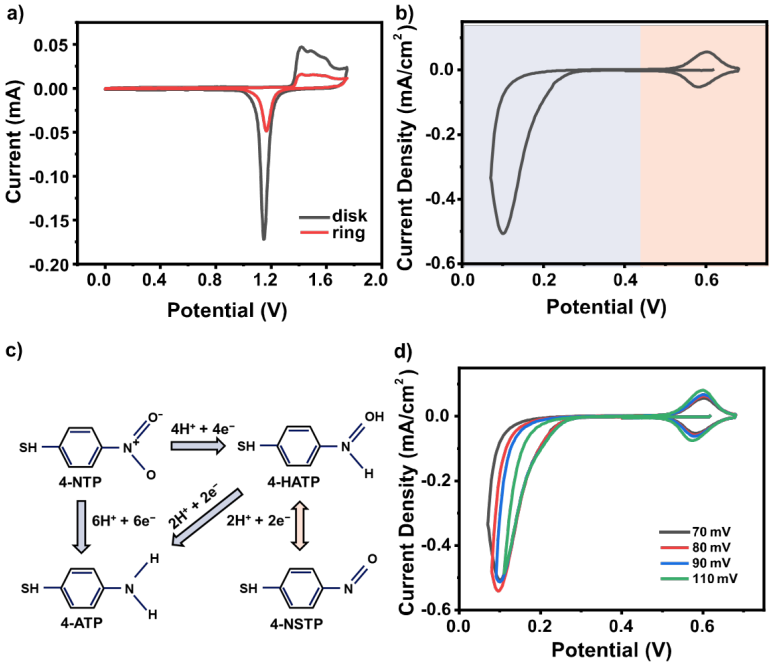

Figure S1. a) Blank voltammograms of the ring (black) and disc (red) electrodes taken in 0.1 M H_2SO_4 at 100 mV s^{-1} . **b)** the Voltammogram of conversion from 4-NTP to the4-NSTP/4-HATP redox couple in Ar-saturated 0.1M H_2SO_4 at 100mV/s.**c)** scheme of the reduction pathways of 4-NTP; **d)** Reduction of 4-NTP with different vertex potentials during cyclic voltammetry in Ar-saturated 0.1M H_2SO_4 at 100mV/s.

Calibration Curve

The peak potentials of the pH redox couple were measured by cyclic voltammetry in electrolytes with different pH. The alkaline region was measured in 0.1 M $KHCO_3$ with pH adjusted by adding KOH or purging CO_2. The acidic region was measured in CO_2 saturated 0.1 M $NaClO_4$. pH was measured by a pH meter (lab 855, SI Analytics)

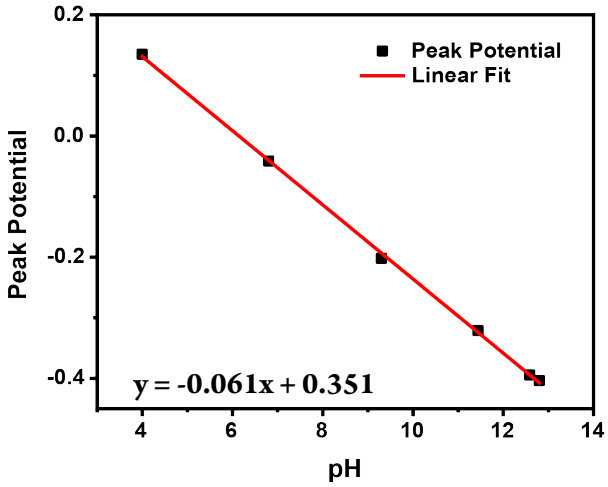

Figure S2. Calibration curve of the 4-NSTP/4-HATP redox couple.

Calculation of the interfacial pH

The interfacial pH at the disk was deduced from the peak potential of the 4-NSTP/4-HATP pH sensing couple. During RRDE measurements, cyclic voltammograms of the 4-HATP/4-NSTP modified Au ring were constantly recorded, the peak potentials of which shifted negatively with the increasing pH (Figure S3a). Firstly, these peak potentials were determined by fitting the anodic scans with a Gaussian function with a linear background. Using the calibration curve (pH_{RING} = (0.351 − E)/ 0.061, see Figure S2b), interfacial pH on the ring electrode was obtained from the peak potential (Figure S3b). Then, the interfacial pH of the disk electrode was calculated according to the well-defined concentration profile of RRDE, developed from the convective diffusion equation by Albery and Calvo. [3] The ratio between the average concentration of products on the ring and the disk is defined as the detection efficiency N_D (Eq. s2), where μ is the normalized concentration of products (Eq. s1), C_∞ is the bulk concentration and subscripts “d” and “r” stand for the ring and disk electrode, respectively. N_D depends only on the geometry of the electrode (Eqs. s3-4),

where r_1, r_2 and r_3 are the radii of the disk, the inner ring and the outer ring, respectively. [4] In our case, the designated product here is OH^-. As the current on the ring is far smaller than on the disk, it is assumed that the electric field from the ring barely influences the concentration profile of OH^-. Under strong polarization in highly conductive electrolytes, the current distribution within the disk is assumed to be uniform. [5] Consequently, the N_D of the RRDE tip employed here (r_1 = 5.0 mm, r_2 = 6.5 mm, r_3 = 7.5 mm) is calculated to be 0.23 according to Eq. s4.

However, in CO_2-saturated bicarbonates, OH^- generated on the disk is partially consumed by either CO_2 or HCO_3^- on its way to the ring. To avoid an underestimation of the interfacial pH on the disk, these homogeneous buffering reactions (Eqs 2 and 4) are taken into account. [6] With effective buffering from CO_2/HCO_3^- and HCO_3^-/CO_3^{2-}, autoprotolysis of water is ignored here. Therefore, the normalized concentration μ here was defined as Eq. s5 and the equation for N_D was also modified (Eq. s6). As CO_2 is continuously purged into the electrolyte during the measurements, the total carbon concentration (TC, see Eq. s7), which is the sum of the concentration of the intrinsic bicarbonate electrolyte and the saturated CO_2 concentration from extrinsic bubbling, stays constant (the TCs for 0.1, 0.25, 0.4 and 0.5 M bicarbonate under continuous CO_2 bubbling are 0.135, 0.271, 0.429, 0.526 M respectively). [7] Concentrations of the different carbonaceous species were estimated as a function of pH (Eqs. s8-s10) by combining equilibrium constants from Eq. 2 and 4 and Eq. s7($K_2 = \frac{[H^+][HCO_3^-]}{[CO_2]}$, pK_2 = 6.35, $K_4 = \frac{[H^+][CO_3^{2-}]}{[HCO_3^-]}$, pK_2 = 10.33). [7] As a result, the interfacial pH of the disk electrode was derived from Eqs. S6-s10. The theoretical correlation between the pH on the ring and disk is plotted in Figure S3c. The appearance of two turning points is related to the two buffers in the electrolyte.

$$\mu = (C - C_\infty)/C_\infty \tag{s1}$$

$$N_D = \frac{\mu_r}{\mu_{D,0}} = (C_r - C_\infty)/(C_d - C_\infty) \tag{s2}$$

$$F(\theta) = \frac{3^{\frac{1}{2}}}{4\pi} ln\left(\frac{\left(1+\theta^{\frac{1}{3}}\right)^3}{1+\theta}\right) + \frac{3}{2\pi} tan^{-1}\left(\frac{2\theta^{\frac{1}{3}}-1}{3^{\frac{1}{2}}}\right) + \frac{1}{4} \tag{s3}$$

$$N_D = 1 - \frac{1}{6}F\left[\left(\frac{r_2}{r_1}\right)^3 - 1\right] - \frac{2}{3}F\left[\left(\frac{r_2+r_3}{2r_1}\right)^3 - 1\right] - \frac{1}{6}F\left[\left(\frac{r_3}{r_1}\right)^3 - 1\right] \tag{s4}$$

$$\mu_{OH^-} = \frac{\left(C_{OH^-} + C_{HCO_3^-} + 2C_{CO_3^{2-}} - C_{\infty,OH^-} - C_{\infty,HCO_3^-} - 2C_{\infty,CO_3^{2-}}\right)}{\left(C_{\infty,OH^-} + C_{\infty,HCO_3^-} + 2C_{\infty,CO_3^{2-}}\right)} \tag{s5}$$

$$N_D = \frac{\mu_{r,OH^-}}{\mu_{d,OH^-}} = \frac{C_{r,OH^-} + C_{r,HCO_3^-} + 2C_{r,CO_3^{2-}} - C_{\infty,OH^-} - C_{\infty,HCO_3^-} - 2C_{\infty,CO_3^{2-}}}{C_{d,OH^-} + C_{d,HCO_3^-} + 2C_{d,CO_3^{2-}} - C_{\infty,OH^-} - C_{\infty,HCO_3^-} - 2C_{\infty,CO_3^{2-}}} \tag{s6}$$

$$TC = [CO_2] + [HCO_3^-] + [CO_3^{2-}] \quad \text{(s7)}$$

$$[CO_2] = \frac{TC[H^+]^2}{[H^+]^2 + K_2[H^+] + K_2K_4} \quad \text{(s8)}$$

$$[HCO_3^-] = \frac{TC[H^+]^2}{[H^+]^2 + K_2[H^+] + K_2K_4} \quad \text{(s9)}$$

$$[CO_3^{2-}] = \frac{TC[H^+]^2}{[H^+]^2 + K_2[H^+] + K_2K_4} \quad \text{(s10)}$$

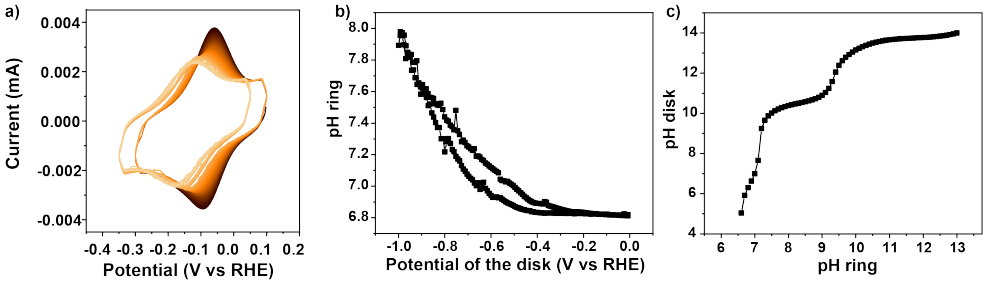

Figure S3. a) Cyclic voltammograms of 4-HATP/4-NSTP modified Au ring electrode during CO_2RR on Au disk electrode in CO_2 saturated 0.1 M $NaHCO_3$ at 2 mV s^{-1} and a rotation rate of 2500 rpm. As the disk was cycling from 0 to – 1.0 V vs RHE, the CVs on the ring evolved from dark red to light and the peak potentials shifted negatively. **b)** Variation of interfacial pH at the ring obtained from peak potentials from a) via calibration curve. **c)** The correspondence between pH_{ring} and pH_{disk} in in CO_2 saturated bicarbonates.

B

Comparison of our RRDE pH sensor and IrOx

The accuracy and sensitivity of the RRDE pH sensor is highly dependent on the pH-sensitive molecule (or material) present on the ring. Compared with, for example, the recently published IrOx probe from Tackett and co-workers, [8] our pH sensor is endowed with higher sensitivity, stability and reproducibility, and wider working range. A direct comparison regarding different properties is given in Table S1 below:

Table S1. Comparison of the pH sensor used by Tackett et al. and in this work:

	This work	**Tackett et al. [8]**
pH-sensitive molecule	4-HATP/4-NSTP redox couple	IrO_x
Signal monitored	Current (voltammetric)	Open circuit potential (Potentiometric)
Type of material	Self-assembled monolayer	µm-thick oxide film
Time resolution	4s per data point	120s per data point
Working range	pH 1-13	pH 2-12
Stability	High (no need of reactivation or recalibration)	Dependent on the quality of the IrO_x film[9, 10] Possible dissolution in acidic media[11]
Reproducibility	High[2]	Dependent on the quality of the IrO_x film pH probe needs calibration every day
Sensitivity	0.1 pH unit[2]	n.a.

Scan rate dependence experiments in bicarbonate electrolyte

To confirm the equilibrium assumption mentioned above, variations of interfacial pH were recorded with higher scan rates on the disk in CO_2 saturated bicarbonates. As shown in Figure S4a-S4b, the current density increases with scan rate. As a result, accumulation of OH^- near the interface of the electrode increases with scan rate, leading to a higher interfacial pH. The interference from current density makes it difficult to distinguish the scan rate effect.

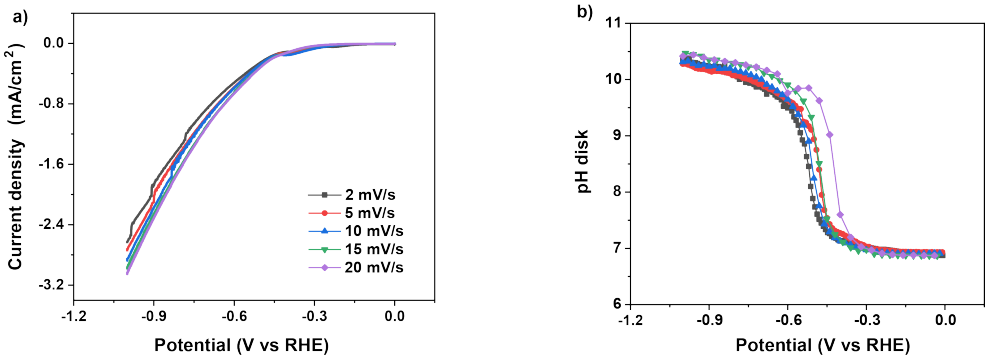

Figure S4. a) Cyclic voltammograms in CO_2 saturated 0.1 M $NaHCO_3$ at different scan rates. The rotation rate of RRDE is 2500 rpm. **b)** Variation of the interfacial pH as a function of potential during cyclic voltammetry in figure 4a.

Calculation of theoretical limiting current density and thickness of diffusion layer

The limiting current density for CO_2RR (J_L) and thickness of diffusion layer (δ) is calculated according to the Levich equation:

$$J_L = -0.62nFD^{2/3}\omega^{1/2}\upsilon^{-1/6}C^*$$

$$\delta = 1.61D^{1/3}\omega^{-1/2}\upsilon^{1/6}$$

where *n* is the number of electrons transferred, *F* is the Faraday constant (C mol^{-1}), *D* is the diffusion coefficient (cm^2 s $^{-1}$), ω is the angular rotation rate (rad s^{-1}), *v* is the kinematic viscosity (cm^2 s $^{-1}$) and *C* is the bulk concentration of the reactant (mol cm^{-3}). For CO_2RR, *n* is equal to 2. The diffusion coefficient *D* is 1.95*10^{-5} cm^2 s $^{-1}$. The kinematic viscosity of water is 0.0089 cm^2 s^{-1}. The angular rotation rate of 2500 RPM corresponds to 261.8 rad s^{-1}. The bulk concentration of CO_2 is 35 mM. The calculated limiting current density is 101.41 mA cm^{-2}. The thickness of diffusion layer is 12.24 µm.

Variation of concentrations of the carbonaceous species

Variation of concentrations of the carbonaceous species is calculated from the interfacial pH monitored under different conditions. According to the results mentioned above, the current density range can be divided into two parts. In the first range (log j < –1.0 mA cm^{-2}), the interfacial pH is buffered by CO_2/HCO_3^- couple, while the in the second range, the

interfacial pH is buffered by HCO_3^-/CO_3^{2-} couple. The results show that increasing mass transport, buffer capacity, and the size and the concentration of cation can resist the variation of interfacial pH: exhaustion of CO_2 and accumulation of HCO_3^- in the CO_2/HCO_3^-

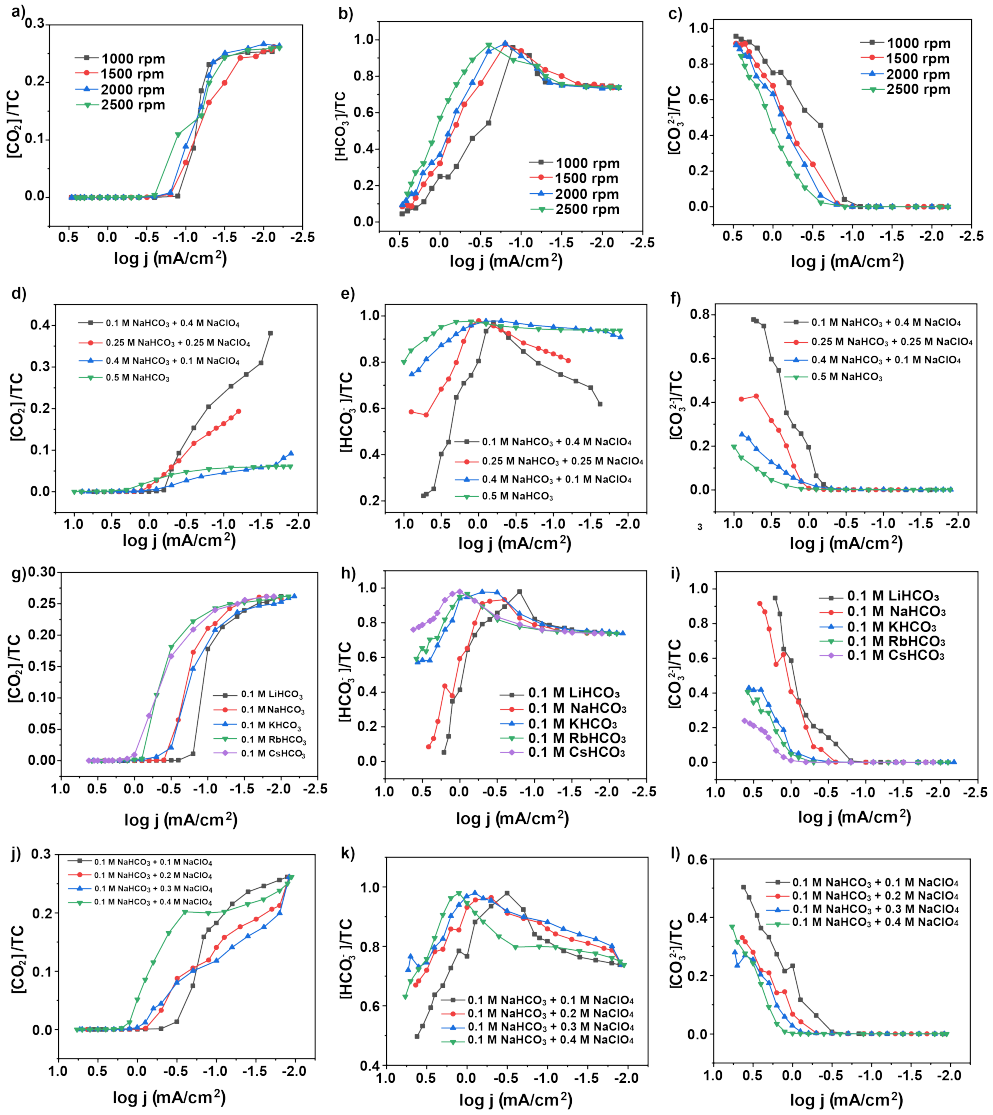

Figure S5. Variation of the interfacial pH as a function of the logarithm of the current density during cyclic voltammetry in **(a-c)** CO_2 saturated 0.1 M $NaHCO_3$ with different rotation rates, **(d-f)** CO_2 saturated bicarbonate with different buffer capacities, **(g-i)** CO_2 saturated bicarbonate with different cations, and **(j-m)** CO_2 saturated bicarbonate with different Na^+ concentrations. The

buffer range is postponed, and consumption of HCO_3^- and generation of CO_3^{2-} in the HCO_3^-

/CO_3^{2-} buffer range is slowed down as well.

References

(1)L.-B. Zhao, J.-L. Chen, M. Zhang, D.-Y. Wu and Z.-Q. Tian, *The Journal of Physical Chemistry C*, 2015, **119**, 4949-4958.

(2)M. C. O. Monteiro, L. Jacobse, T. Touzalin and M. T. M. Koper, *Anal Chem*, 2020, **92**, 2237-2243.

(3)W. Albery, *Transactions of the Faraday Society*, 1966, **62**, 1915-1919.

(4)W. J. Albery and E. J. Calvo, *Journal of the Chemical Society, Faraday Transactions 1: Physical Chemistry in Condensed Phases*, 1983, **79**, 2583-2596.

(5)W. J. Albery and M. L. Hitchman, *Ring-disc Electrodes [by] W.J. Albery and M.L. Hitchman*, Clarendon Press, 1971.

(6)R. E. Zeebe and D. Wolf-Gladrow, *CO2 in seawater: equilibrium, kinetics, isotopes*, Gulf Professional Publishing, 2001.

(7)H. Zhong, K. Fujii, Y. Nakano and F. Jin, *The Journal of Physical Chemistry C*, 2014, **119**, 55-61.

(8)B. M. Tackett, D. Raciti, N. W. Brady, N. L. Ritzert and T. P. Moffat, *The Journal of Physical Chemistry C*, 2022, **126**, 7456-7467.

(9)P. Steegstra and E. Ahlberg, *Journal of Electroanalytical Chemistry*, 2012, **685**, 1-7.

(10)P. Steegstra and E. Ahlberg, *Electrochimica Acta*, 2012, **76**, 26-33.

(11)P. Jovanovič, N. Hodnik, F. Ruiz-Zepeda, I. Arčon, B. Jozinović, M. Zorko, M. Bele, M. Šala, V. S. Šelih and S. Hočevar, *Journal of the American Chemical Society*, 2017, **139**, 12837-12846.

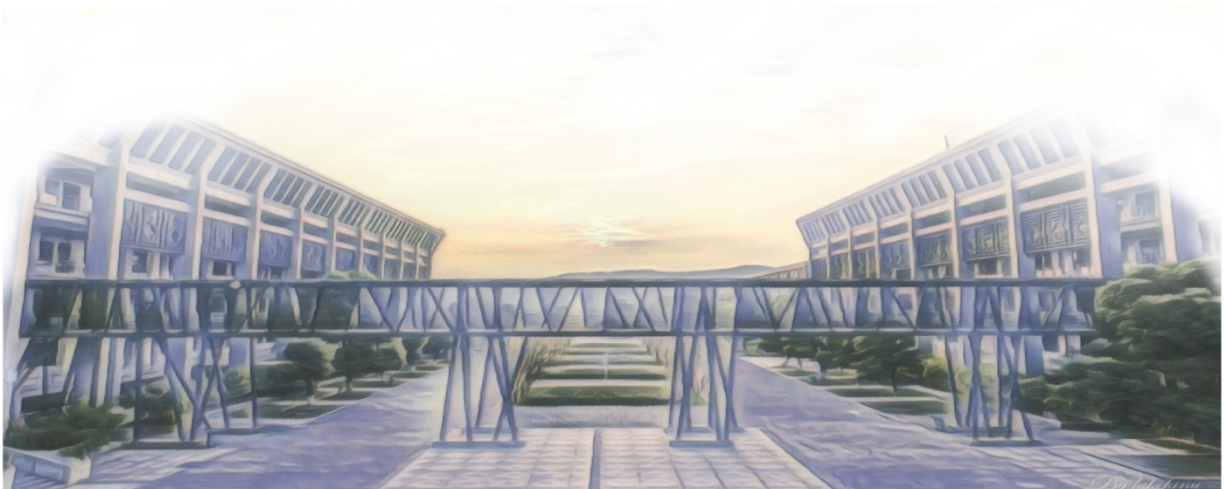

Appendix C

Supporting Information to Chapter 4

Characterization of the Au disk and ring electrode

The Au disk and ring electrode were characterized by cyclic voltammetry in 0.1 M H_2SO_4 respectively, to inspect possible variation of the electrode surface due to the interfacial pH measurements and the dopamine coating. As shown in Figure S1a-b, the CVs before and after dopamine coating on Au ring and disk electrode agree well with each other, signifying that dopamine residue has been totally removed and this coating process hardly influences the surface of Au ring and disk electrode. Figure s1c demonstrates that no discernable changes was traced on the surface of the Au disk during interfacial pH and FE measurements. As the peaks observed in the CVs signify the interplay between Au surface atoms, OH_{ads} and O_{ads} as well as the formation of Au oxide, they are surface sensitive. Each facet exhibits unique peak signatures. Since there is no observable deviation in the CVs, we conclude that the surface structure remains unchanged.

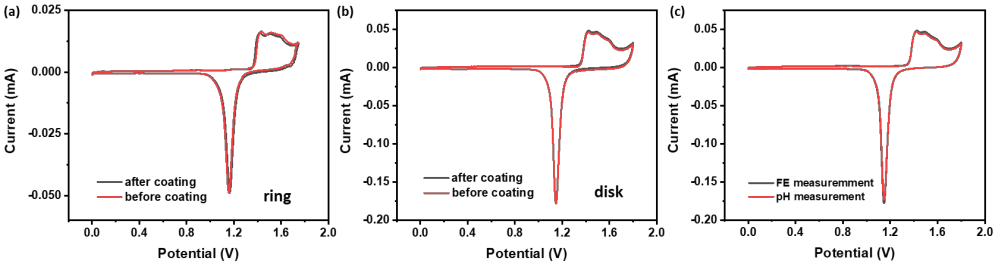

Figure S1. Cyclic voltammograms of **a)** the Au ring and **b)** the Au disk recorded in Ar-saturated 0.1 M H_2SO_4 at 100 mV s^{-1} before and after the dopamine coating. **c)** Cyclic voltammograms the Au ring and the Au disk recorded in Ar-saturated 0.1 M H_2SO_4 at 100 mV s^{-1} before the interfacial pH measurement and the FE measurement.

Calculation of the interfacial pH on the disk

Peak potentials of the 4-NSTP/4-HATP redox couple during CO2RR on the Au disk was recorded. According to the calibration curve of the redox couple (Figure S2a), the interfacial pH on the ring electrode can be obtained. To calculate the interfacial pH on the disk electrode, the relationship between pH on the ring and pH on the disk needs to be figured out. According to the convective-diffusion equation of RRDE, the ratio of the average concentration of products on the ring and the disk is defined to be the detection efficiency N_D as displayed in Eq. s2, [1] where μ is the normalized concentration of products (Eq. s1),

C_∞ is the bulk concentration (The subscript "d" and "r" symbolize the ring and disk electrode, respectively). N_D is determined by the geometry of the electrode (Eqs. s3-4), in which r_1, r_2 and r_3 are the radii of the disk, the inner ring and the outer ring, respectively. [2] In this work, the N_D of the RRDE tip employed here (r_1 = 5.0 mm, r_2 = 6.5 mm, r_3 = 7.5 mm) is 0.23.

Besides, the homogenous reactions involving protons or hydroxyl ions also impact the pH gradient between ring and disk electrode. In CO_2-saturated perchlorate, when the interfacial environment turns alkaline, OH^- generated on the disk is partially consumed by either CO_2 or HCO_3^- on its way to the ring. Also, in CO_2-saturated electrolyte with protic anions, such as HSO_4^{2-} $H_2PO_4^-$ in this work, the OH^- generated by CO2R is consumed collectively by the protic anions and CO_2 and HCO_3^-.To avoid an underestimation of the interfacial pH on the disk, influences from the homogeneous buffering reactions (Eqs 2 and 4) need to be compensated.[3] For CO_2-saturated perchlorate, the normalized concentration μ here was redefined as Eq. s5 and the equation for N_D was also modified (Eq. s6). As CO_2 is continuously purged into the electrolyte during the measurements, the total carbon concentration (TC, see Eq. s7), which is the sum of the concentration of the intrinsic bicarbonate electrolyte and the saturated CO_2 concentration from extrinsic bubbling, is supposed to be constant throughout the measurements. Hence the TC for 0.1 M perchlorate under continuous CO_2 bubbling is 0.135. Concentrations of the different carbonaceous species were estimated as a function of pH (Eqs. s8-s10) by combining dissociation equilibrium constants of CO_2 (pKc_1 = 6.35, pKc_2 = 10.33). [4] As a result, the interfacial pH of the disk electrode was derived from Eqs. S6-s10. The theoretical correlation between the pH on the ring and disk in 0.1 M Sodium perchlorate is plotted in Figure S2b.

$$\mu = (C - C_\infty)/C_\infty \tag{s1}$$

$$N_D = \frac{\mu_r}{\mu_{D,0}} = (C_r - C_\infty)/(C_d - C_\infty) \tag{s2}$$

$$F(\theta) = \frac{3^{\frac{1}{2}}}{4\pi}\ln\left(\frac{\left(1+\theta^{\frac{1}{3}}\right)^3}{1+\theta}\right) + \frac{3}{2\pi}\tan^{-1}\left(\frac{2\theta^{\frac{1}{3}}-1}{3^{\frac{1}{2}}}\right) + \frac{1}{4} \tag{s3}$$

$$N_D = 1 - \frac{1}{6}F\left[\left(\frac{r_2}{r_1}\right)^3 - 1\right] - \frac{2}{3}F\left[\left(\frac{r_2+r_3}{2r_1}\right)^3 - 1\right] - \frac{1}{6}F\left[\left(\frac{r_3}{r_1}\right)^3 - 1\right] \tag{s4}$$

$$\mu_{OH^-} = \frac{\left(C_{OH^-} + C_{HCO_3^-} + 2C_{CO_3^{2-}} - C_{\infty,OH^-} - C_{\infty,HCO_3^-} - 2C_{\infty,CO_3^{2-}}\right)}{\left(C_{\infty,OH^-} + C_{\infty,HCO_3^-} + 2C_{\infty,CO_3^{2-}}\right)} \tag{s5}$$

$$N_D = \frac{\mu_{r,OH^-}}{\mu_{d,OH^-}} = \frac{C_{r,OH^-} + C_{r,HCO_3^-} + 2C_{r,CO_3^{2-}} - C_{\infty,OH^-} - C_{\infty,HCO_3^-} - 2C_{\infty,CO_3^{2-}}}{C_{d,OH^-} + C_{d,HCO_3^-} + 2C_{d,CO_3^{2-}} - C_{\infty,OH^-} - C_{\infty,HCO_3^-} - 2C_{\infty,CO_3^{2-}}} \tag{s6}$$

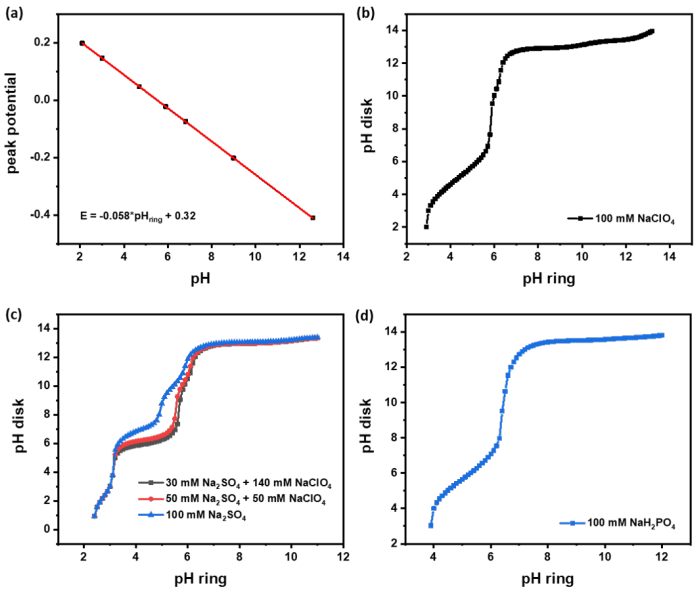

Figure S2. **a)** Calibration curve of the 4-NSTP/4-HATP redox couple measured in 0.1 M Na_2SO_4, pH is adjusted by adding H_2SO_4 or NaOH. The correspondence between pH_{ring} and pH_{disk} in CO_2-saturated **b)** 0.1 M $NaClO_4$ (pH=3), **c)** Na_2SO_4 with 200 mM Na^+ and different SO_4^{2-} concentrations (pH=3), and **d)** 0.1 M NaH_2PO_4 (pH=4).

$$TC = [CO_2] + [HCO_3^-] + [CO_3^{2-}] \quad (s7)$$

$$[CO_2] = \frac{TC[H^+]^2}{[H^+]^2 + K_{c1}[H^+] + K_{c1}K_{c2}} \quad (s8)$$

$$[HCO_3^-] = \frac{TCK_{c1}[H^+]}{[H^+]^2 + K_{c1}[H^+] + K_{c1}K_{c2}} \quad (s9)$$

$$[CO_3^{2-}] = \frac{TCK_{c1}K_{c2}}{[H^+]^2 + K_{c1}[H^+] + K_{c1}K_{c2}} \quad (s10)$$

For CO_2-saturated sulfate, buffering from sulfuric species and carbonate species is compensated, the normalized concentration μ here was redefined as Eq. s11 and the equation for N_D was also modified (Eq. s12). TS is defined as the total concentration of sulfuric species (Eq. s13), and the concentrations of each sulfuric species were estimated as a function of pH (Eqs. s14-s15) by combining dissociation equilibrium constants of HSO_4^- (pK_{S1} = 1.99). As a result, the interfacial pH of the disk electrode was derived from Eqs. s12-

s15. The theoretical correlation between the pH on the ring and disk in sodium sulfate with different SO_4^- concentration is plotted in Figure S2c.

$$\mu_{OH^-} = \frac{\left(C_{OH^-} + C_{HCO_3^-} + 2C_{CO_3^{2-}} + C_{SO_4^{2-}} - C_{\infty,OH^-} - C_{\infty,HCO_3^-} - 2C_{\infty,CO_3^{2-}} - C_{\infty,SO_4^{2-}}\right)}{\left(C_{\infty,OH^-} + C_{\infty,HCO_3^-} + 2C_{\infty,CO_3^{2-}} + C_{\infty,SO_4^{2-}}\right)} \quad (s11)$$

$$N_D = \frac{\mu_{r,OH^-}}{\mu_{d,OH^-}} = \frac{C_{r,OH^-} + C_{r,HCO_3^-} + 2C_{r,CO_3^{2-}} + C_{r,HSO_4^-} - C_{\infty,OH^-} - C_{\infty,HCO_3^-} - 2C_{\infty,CO_3^{2-}} - C_{\infty,SO_4^{2-}}}{C_{d,OH^-} + C_{d,HCO_3^-} + 2C_{d,CO_3^{2-}} + C_{d,SO_4^{2-}} - C_{\infty,OH^-} - C_{\infty,HCO_3^-} - 2C_{\infty,CO_3^{2-}} - C_{\infty,SO_4^{2-}}} \quad (s12)$$

$$TS = [HSO_4^-] + [SO_4^{2-}] \quad (s13)$$

$$[HSO_4^-] = \frac{TS[H^+]}{[H^+] + K_{S1}} \quad (s14)$$

$$[SO_4^{2-}] = \frac{TS[K_{S1}]}{[H^+] + K_{S1}} \quad (s15)$$

Similarly, for CO_2-saturated phosphate, buffering from phosphate species, carbonate species is compensated, the normalized concentration μ here was redefined as Eq. s16 and the equation for N_D was also modified (Eq. s17). TP is defined as the total concentration of sulfuric species (Eq. s18), and the concentrations of each sulfuric species were estimated as a function of pH (Eqs. s19-s21) by combining dissociation equilibrium constants of $H_2PO_4^-$ (pK_{P1} = 2.14 pK_{P2} = 7.20, pK_{P3} = 12.37). Specially, As the measurements in phosphate is performed at bulk pH 4, H_3PO_4 is ignored because of its extremely small concentration to simplify the calculation. The interfacial pH of the disk electrode was derived from Eqs. S18-s21. The theoretical correlation between the pH on the ring and disk in 0.1 M phosphate is plotted in Figure S2d.

$$\mu_{OH^-} = \frac{\left(C_{OH^-} + C_{HCO_3^-} + 2C_{CO_3^{2-}} + C_{HPO_4^{2-}} + 2C_{PO_4^{3-}} - C_{\infty,OH^-} - C_{\infty,HCO_3^-} - 2C_{\infty,CO_3^{2-}} - C_{\infty,HPO_4^{2-}} - 2C_{\infty,PO_4^{3-}}\right)}{\left(C_{\infty,OH^-} + C_{\infty,HCO_3^-} + 2C_{\infty,CO_3^{2-}} + C_{\infty,HPO_4^{2-}} + 2C_{\infty,PO_4^{3-}}\right)} \quad (s16)$$

$$N_D = \frac{\mu_{r,OH^-}}{\mu_{d,OH^-}} =$$

$$\frac{C_{r,OH^-} + C_{r,HCO_3^-} + 2C_{r,CO_3^{2-}} + C_{r,HPO_4^{2-}} + 2C_{r,PO_4^{3-}} - C_{\infty,OH^-} - C_{\infty,HCO_3^-} - 2C_{\infty,CO_3^{2-}} - C_{\infty,HPO_4^{2-}} - 2C_{\infty,PO_4^{3-}}}{C_{d,OH^-} + C_{d,HCO_3^-} + 2C_{d,CO_3^{2-}} + C_{d,HPO_4^{2-}} + 2C_{d,PO_4^{3-}} - C_{\infty,OH^-} - C_{\infty,HCO_3^-} - 2C_{\infty,CO_3^{2-}} - C_{\infty,HPO_4^{2-}} - 2C_{\infty,PO_4^{3-}}} \quad (s17)$$

$$TP = [H_2PO_4^-] + [HPO_4^{2-}] + [PO_4^{3-}] \quad (s18)$$

$$[H_2PO_4^-] = \frac{TP[H^+]^2}{[H^+]^2 + K_{S1}[H^+] + K_{S1}K_{S2}} \quad (s19)$$

$$[HPO_4^{2-}] = \frac{TPK_{S1}[H^+]}{[H^+]^2 + K_{S1}[H^+] + K_{S1}K_{S2}} \quad (s20)$$

$$[PO_4^{3-}] = \frac{TPK_{S1}K_{S2}}{[H^+]^2 + K_{S1}[H^+] + K_{S1}K_{S2}} \quad (s21)$$

Ring pH data

Here we show the ring pH data corresponding to Figures 1a, 2a, 3c, 4a, 5b and 6b. The ring pH is markedly dependent on the electrolyte conditions, in agreement with the disk pH data. Noteworthy, as suggested in Figure S3a-b, the ring pH in the mass transport limited region in Na_2SO_4 is higher than that in $NaClO_4$ (and as a result, the corresponding disk pH is also higher in Na_2SO_4), illustrating the great influence of the current density on corresponding reaction environment during CO2RR. The limiting current density in Na_2SO_4 is higher due to the extra proton flux donated by HSO_4^-, leading to a less acidic reaction environment. Once the ring pH reaches around 6, as shown by the calibration curves in Figure S2, the disk pH rises quickly up to 13, due to the lack of a proper buffer anion and the weak buffer strength of the carbonaceous buffer in the electrolytes.

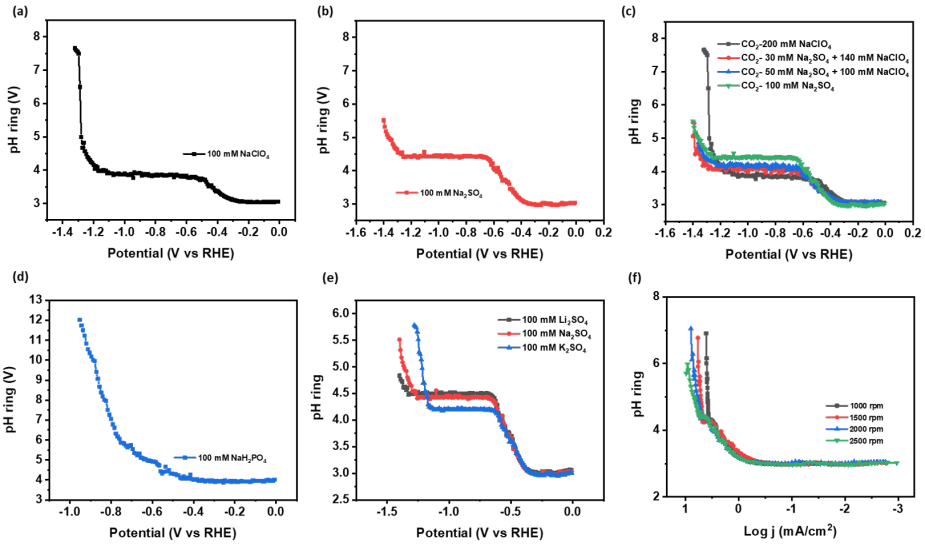

Figure S3. The ring pH data recorded during measurements in **a)** 0.1 M CO_2-saturated $NaClO_4$ with a bulk pH of 3, corresponding to the disk pH data in Figure 1a, **b)** 0.1 M CO_2-saturated Na_2SO_4 with a bulk pH of 3, corresponding to the disk pH data in Figure 2a, **c)** electrolytes with 200 mM Na^+ and different SO_4^{2-} concentrations with a bulk pH of 3, corresponding to the disk pH data in Figure 3c, **d)** 0.1 M CO_2-saturated NaH_2PO_4 with a bulk pH of 4, corresponding to the disk pH data in Figure 4a, **e)** 0.1 M CO_2-saturated sulfate with different cation identity with a bulk pH of 3 corresponding to the disk pH data in Figure 5b, **f)** 0.1 M CO_2-saturated Na_2SO_4 with a bulk pH of 3 with different rotation rates, corresponding to the disk pH data in Figure 6b. The scan rate is 2 mV s^{-1}, and the rotation rate is 2500 rpm unless specially mentioned.

Calculation of Faradaic Efficiency of CO

As a CO-producing metal, Au is also a good catalyst for CO oxidation. [5] Hence the Au ring electrode can easily deconvolute CO from other products on the disk electrode, since H_2 and CO are the only two products generated on the Au planar electrode. The partial current density for CO2RR on the Au disk can be calculated from the experimental ring current (i_{ring}) and the detect efficiency N of the Au ring (Eq. s22).

$$j_{co} = \frac{i_{ring}}{N * ECSA_{disk}} \quad \text{(s22)}$$

The Faradaic efficiency can be calculated by Eq. s23, where the i_{disk} is the current obtained on the disk during experiments.

$$FE_{co} = \frac{i_{ring}}{N * |i_{disk}|} * 100\% \quad \text{(s23)}$$

The partial current density and Faradaic efficiency of HER can be determined from Eq. s23-24

$$j_{H_2} = j_{tot} - j_{co} \quad \text{(s24)}$$

$$FE_{H_2} = 100\% - FE_{co} \quad \text{(s25)}$$

As mentioned in the experimental section, after finishing FE and interfacial pH measurements, the collection efficiency N was measured in 5 mM $K_3Fe(CN)_6$ dissolved in 0.1 M $NaHCO_3$, during which the disk was cycled from 0.27 to 1.27 V vs RHE, while the ring potential was set to 0.96 V vs RHE. The collection efficiency was determined for each rotation rate and was calculated according to Eq. s26.

$$N = \left|\frac{i_{ring}}{i_{disk}}\right| \quad \text{(s26)}$$

FE measurements during chronoamperometry

To confirm the stability of the Au ring CO sensor, FE measurements during chronoamperometry were conducted in 0.1 M CO_2-saturated Na_2SO_4, where CO2RR on the disk electrode is turned ‘‘on’’ and ‘‘off’’ at different potentials from − 0.3 V to − 1.4 V vs RHE every 200s. The rotation rate of RRDE is 2500 rpm. As depicted in Figure S4, the results agree well with the ones during cyclic voltammetry in Figure 2. FE of CO2RR increases up to ~60% along the mass transport-limited region (from − 0.6V ~ −1.2 V), and starts to decay once the water reduction sets in. During steady-state electrolysis, the ring current stays stable.

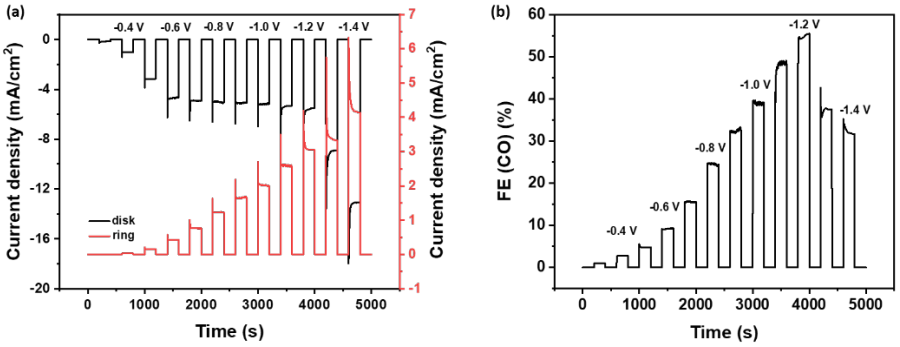

Figure S4. **a)** Current density on the disk (black curve) and ring (black curve) and **b)** FE of CO during chronoamperometry in 0.1 M CO_2-saturated Na_2SO_4 (pH=3).

Reference

(1)Albery, W., Ring-disc electrodes. Part 1.—A new approach to the theory. *Transactions of the Faraday Society* **1966,** *62*, 1915-1919.

(2)Albery, W. J.; Calvo, E. J., Ring–disc electrodes. Part 21.—pH measurement with the ring. *Journal of the Chemical Society, Faraday Transactions 1: Physical Chemistry in Condensed Phases* **1983,** *79* (11), 2583-2596.

(3)Zeebe, R. E.; Wolf-Gladrow, D., *CO2 in seawater: equilibrium, kinetics, isotopes*. Gulf Professional Publishing: 2001.

(4)Zhong, H.; Fujii, K.; Nakano, Y.; Jin, F., Effect of CO2 Bubbling into Aqueous Solutions Used for Electrochemical Reduction of CO2 for Energy Conversion and Storage. *The Journal of Physical Chemistry C* **2014,** *119* (1), 55-61.

(5)Monteiro, M. C. O.; Jacobse, L.; Koper, M. T. M., Understanding the Voltammetry of Bulk CO Electrooxidation in Neutral Media through Combined SECM Measurements. *J Phys Chem Lett* **2020,** *11* (22), 9708-9713.

(6)Blizanac, B. B.; Arenz, M.; Ross, P. N.; Marković, N. M., Surface Electrochemistry of CO on Reconstructed Gold Single Crystal Surfaces Studied by Infrared Reflection Absorption Spectroscopy and Rotating Disk Electrode. *J. Am. Chem. Soc.* **2004,** *126* (32), 10130-10141.

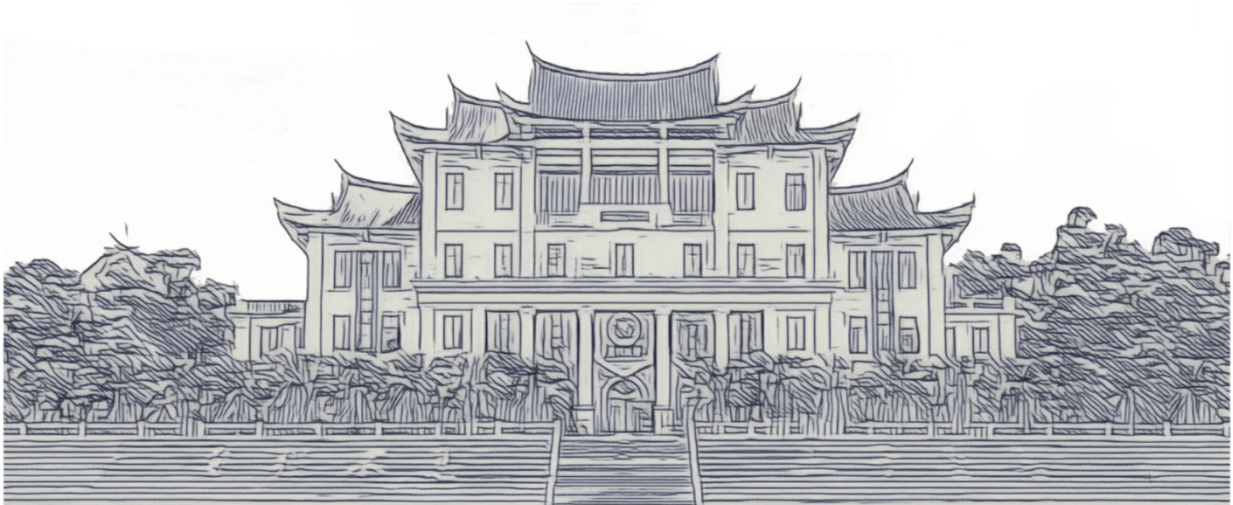

Appendix D

Supporting Information to Chapter 5

Bulk pH of the electrolytes employed in the quantitative analysis

Table 1 Bulk pH of electrolytes employed in measurements of Figure 3

Electrolyte	Bulk pH
100 mM $LiClO_4$ + 0 mM Li_2SO_4	3.964
95 mM $LiClO_4$ + 5 mM Li_2SO_4	3.964
85 mM $LiClO_4$ + 15 mM Li_2SO_4	3.967
70 mM $LiClO_4$ + 30 mM Li_2SO_4	3.964
55 mM $LiClO_4$ + 45 mM Li_2SO_4	3.964
40 mM $LiClO_4$ + 60 mM Li_2SO_4	3.957
25 mM $LiClO_4$ + 75 mM Li_2SO_4	3.964
0 mM $LiClO_4$ + 100 mM Li_2SO_4	3.960

Table 2 Bulk pH of electrolytes employed in measurements of Figure 4

Electrolyte	Bulk pH
100 mM $LiClO_4$ + 0 mM $KClO_4$	3.955
95 mM $LiClO_4$ + 5 mM $KClO_4$	3.948
85 mM $LiClO_4$ + 15 mM $KClO_4$	3.950
70 mM $LiClO_4$ + 30 mM $KClO_4$	3.965
55 mM $LiClO_4$ + 45 mM $KClO_4$	3.948
40 mM $LiClO_4$ + 60 mM $KClO_4$	3.954
25 mM $LiClO_4$ + 75 mM $KClO_4$	3.948

Table 3 Bulk pH of electrolytes employed in measurements of Figure 5

Electrolyte	Bulk pH
100 mM $LiClO_4$ + 0 mM $CsClO_4$	3.951
95 mM $LiClO_4$ + 5 mM $CsClO_4$	3.949
85 mM $LiClO_4$ + 15 mM $CsClO_4$	3.944
70 mM $LiClO_4$ + 30 mM $CsClO_4$	3.940
55 mM $LiClO_4$ + 45 mM $CsClO_4$	3.943
40 mM $LiClO_4$ + 60 mM $CsClO_4$	3.943
25 mM $LiClO_4$ + 75 mM $CsClO_4$	3.948

Table 4 Bulk pH of electrolytes employed in measurements of Figure 6

Electrolyte	Bulk pH
100 mM Li_2SO_4 + 0 mM K_2SO_4	3.954
95 mM Li_2SO_4 + 5 mM K_2SO_4	3.949
85 mM Li_2SO_4 + 15 mM K_2SO_4	3.955
70 mM Li_2SO_4 + 30 mM K_2SO_4	3.958
55 mM Li_2SO_4 + 45 mM K_2SO_4	3.952
40 mM Li_2SO_4 + 60 mM K_2SO_4	3.953
25 mM Li_2SO_4 + 75 mM K_2SO_4	3.954

Table 5 Bulk pH of electrolytes employed in measurements of Figure 7

Electrolyte	Bulk pH
100 mM Li_2SO_4 + 0 mM Cs_2SO_4	3.961
95 mM Li_2SO_4 + 5 mM Cs_2SO_4	3.953
85 mM Li_2SO_4 + 15 mM Cs_2SO_4	3.965
70 mM Li_2SO_4 + 30 mM Cs_2SO_4	3.959
55 mM Li_2SO_4 + 45 mM Cs_2SO_4	3.960
40 mM Li_2SO_4 + 60 mM Cs_2SO_4	3.965
25 mM Li_2SO_4 + 75 mM Cs_2SO_4	3.962

Table 6 Bulk pH of electrolytes employed in measurements of Figure S7a

Electrolyte	Bulk pH
100 mM $LiClO_4$ + 0 mM $NaClO_4$	3.960
95 mM $LiClO_4$ + 5 mM $NaClO_4$	3.960
85 mM $LiClO_4$ + 15 mM $NaClO_4$	3.967
70 mM $LiClO_4$ + 30 mM $NaClO_4$	3.965
55 mM $LiClO_4$ + 45 mM $NaClO_4$	3.961
40 mM $LiClO_4$ + 60 mM $NaClO_4$	3.969
25 mM $LiClO_4$ + 75 mM $NaClO_4$	3.961

Table 7 Bulk pH of electrolytes employed in measurements of Figure S7b-d

Electrolyte	Bulk pH
100 mM Li_2SO_4 + 0 mM Na_2SO_4	3.954
95 mM Li_2SO_4 + 5 mM Na_2SO_4	3.955
85 mM Li_2SO_4 + 15 mM Na_2SO_4	3.951
70 mM Li_2SO_4 + 30 mM Na_2SO_4	3.957
55 mM Li_2SO_4 + 45 mM Na_2SO_4	3.968
40 mM Li_2SO_4 + 60 mM Na_2SO_4	3.963
25 mM Li_2SO_4 + 75 mM Na_2SO_4	3.970

Table 8 Bulk pH of electrolytes employed in measurements of Figure S8-9

Electrolyte	Bulk pH
100 mM Li_2SO_4 + 0 mM Na_2SO_4	3.701
95 mM Li_2SO_4 + 5 mM Na_2SO_4	3.705
85 mM Li_2SO_4 + 15 mM Na_2SO_4	3.695
70 mM Li_2SO_4 + 30 mM Na_2SO_4	3.699
55 mM Li_2SO_4 + 45 mM Na_2SO_4	3.698
40 mM Li_2SO_4 + 60 mM Na_2SO_4	3.703
25 mM Li_2SO_4 + 75 mM Na_2SO_4	3.700

A quantitative analysis of the steady-state behavior of HER coupled with pre-chemical processes

Dating back to the pioneering work by Koutecký and Levich in 1958, [1] extensive efforts have been devoted to evaluating the current response of steady-state HER when coupled to a pre-chemical process. [2-4] Rebouillat et al [5] developed a mathematical analysis for different rate-limiting scenarios, dependent on the competition between the chemical reaction kinetics and diffusion. According to our measurements, the steady-state behavior under our conditions belongs to their "DM" regime, where the reaction rate is still controlled by diffusion but modified by the chemical process, in our case the dissociation of HSO_4^- and hydrolysis of K^+ and Cs^+. The current response is evaluated through Eq. s1,

$$\frac{1}{i} = \frac{\omega^{-1/2}}{0.62nFAD_{HA}^{2/3}\upsilon^{-1/6}KC_{\Sigma}} \quad \text{(s1)}$$

where n is the number of electrons transferred, F is the Faraday constant (C mol^{-1}), D_{HA} is the diffusion coefficient of the electroinactive species (cm^2 s $^{-1}$), ω is the angular rotation

rate (rad s^{-1}), v is the kinematic viscosity (cm^2 s^{-1}), K is the dissociation constant of the proton donor and C_Σ is the total concentration of the proton donor.

To account for the influence of the bulk proton concentration, which is relevant in our case, an additional current from the bulk protons is introduced in Eq. s2,

$$\frac{1}{i} = \frac{\omega^{-1/2}}{0.62nFAD_{HA}^{2/3}\upsilon^{-1/6}KC_\Sigma + 0.62nFAD_H^{2/3}\upsilon^{-1/6}C_H} \quad \text{(s2)}$$

where D_H is the diffusion coefficient of the proton (cm^2 s^{-1}) and C_H is the bulk concentration of the proton (mol cm^{-3}). This implies a linear relationship between inverse limiting current density and the inverse square root of rotation speed with a Koutechy-Levich Slope (Eq. s3, referred to as "$S_{K\text{-}L}$" in the following text).

$$S_{K-L}{}^{-1} = 0.62nFAD_{HA}^{2/3}\upsilon^{-1/6}KC_\Sigma + 0.62nFAD_H^{2/3}\upsilon^{-1/6}C_H \quad \text{(s3)}$$

The inverse $S_{K\text{-}L}$ is linearly dependent the concentration of the electroinactive species, from which the corresponding acid-base constant K can be evaluated.

In case both anionic and cationic proton donors are present, a third term needs to be introduced in the analysis to account for both the influence of the alkali cation and of HSO_4^- (Eqs. s4-5),

$$\frac{1}{i} = \frac{\omega^{-1/2}}{0.62nFAD_{cat}^{2/3}\upsilon^{-1/6}K_{cat}C_{cat} + 0.62nFAD_{HSO_4^-}^{2/3}\upsilon^{-1/6}K_{HSO_4^-}C_{(H)SO_4^-} + 0.62nFAD_H^{2/3}\upsilon^{-1/6}C_H} \quad \text{(s4)}$$

$$S_{K-L}{}^{-1} = 0.62nFAD_{cat}^{2/3}\upsilon^{-1/6}K_{cat}C_{cat} + 0.62nFAD_H^{2/3}\upsilon^{-1/6}C_H + 0.62nFAD_{HSO_4^-}^{2/3}\upsilon^{-1/6}K_{HSO_4^-}C_{(H)SO_4^-} \quad \text{(s5)}$$

where $D_{HSO_4^-}$ is the diffusion coefficient of HSO_4^- (cm^2 s^{-1}) and $D_{HSO_4^-}$ is the bulk concentration of HSO_4^- (mol cm^{-3}). Similarly, the inverse $S_{K\text{-}L}$ here is linearly dependent on the concentration of the electroinactive species, from which the K's of both the cation and the $D_{HSO_4^-}$ can be evaluated.

The polarization curves recorded in different electrolyte conditions with rotation rates from 900 rpm to 2500 rpm are shown in Figure S1-7. For HER, n is equal to 1 per proton. The Faraday constant is 96485 C mol^{-1}. The diffusion coefficients of $D_{HSO_4^-}$, D_{K^+} and D_{Cs^+} are 1.385×10^{-5} cm^2 s^{-1}, 1.957×10^{-5} cm^2 s^{-1}, 2.056×10^{-5} cm^2 s^{-1}. [6] The kinematic viscosity of water is 0.0089 cm^2 s^{-1}.

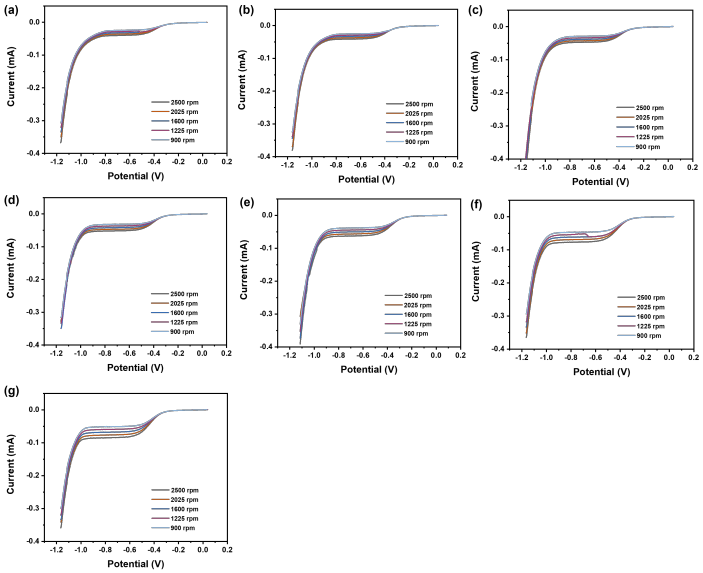

Figure S1. **a-g)** Polarization curves recorded on a Au RDE at 10 mV s^{-1} with rotation rates from 900 rpm to 2500 rpm at a bulk pH of 4 in Ar-saturated 0 mM, 5 mM, 15 mM, 30 mM, 45 mM, 60 mM, 75 mM Li_2SO_4 respectively, $LiClO_4$ was added to adjust the ionic strength.

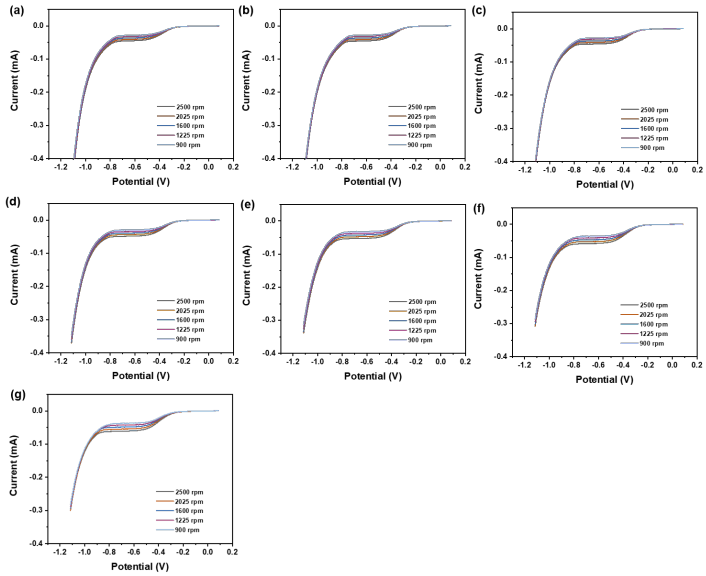

Figure S2. **a-g)** Polarization curves recorded on a Au RDE at 10 mV s^{-1} with rotation rates from 900 rpm to 2500 rpm at a bulk pH of 4 in Ar-saturated 0 mM, 5 mM, 15 mM, 30 mM, 45 mM, 60 mM, 75 mM $KClO_4$ respectively, $LiClO_4$ was added to adjust the ionic strength.

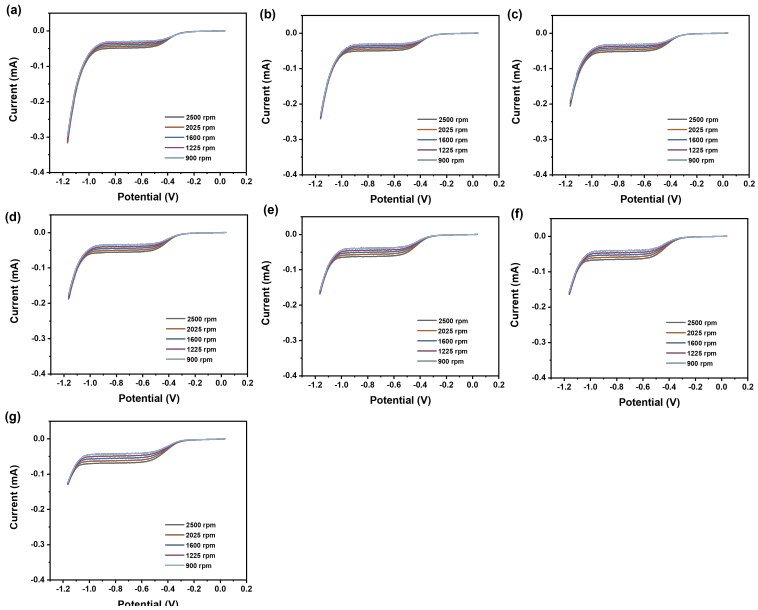

Figure S3. **a-g)** Polarization curves recorded on a Au RDE at 10 mV s^{-1} with rotation rates from 900 rpm to 2500 rpm at a bulk pH of 4 in Ar-saturated 0 mM, 5 mM, 15 mM, 30 mM, 45 mM, 60 mM, 75 mM $CsClO_4$ respectively, $LiClO_4$ was added to adjust the ionic strength.

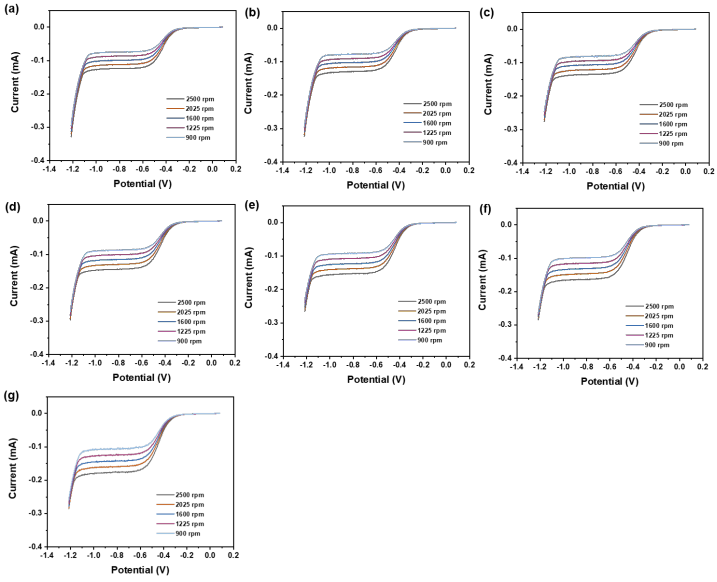

Figure S4. **a-g)** Polarization curves recorded on a Au RDE at 10 mV s^{-1} with rotation rates from 900 rpm to 2500 rpm at a bulk pH of 4 in Ar-saturated 0 mM, 5 mM, 15 mM, 30 mM, 45 mM, 60 mM, 75 mM K_2SO_4 respectively, Li_2SO_4 was added to adjust the ionic strength.

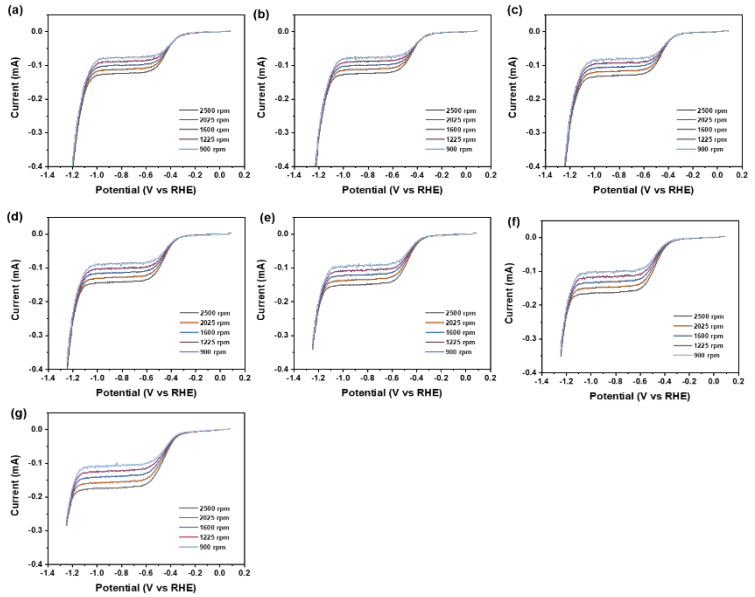

Figure S5. **a-g)** Polarization curves recorded on a Au RDE at 10 mV s^{-1} with rotation rates from 900 rpm to 2500 rpm at a bulk pH of 4 in Ar-saturated 0 mM, 5 mM, 15 mM, 30 mM, 45 mM, 60 mM, 75 mM Cs_2SO_4 respectively, Li_2SO_4 was added to adjust the ionic strength.

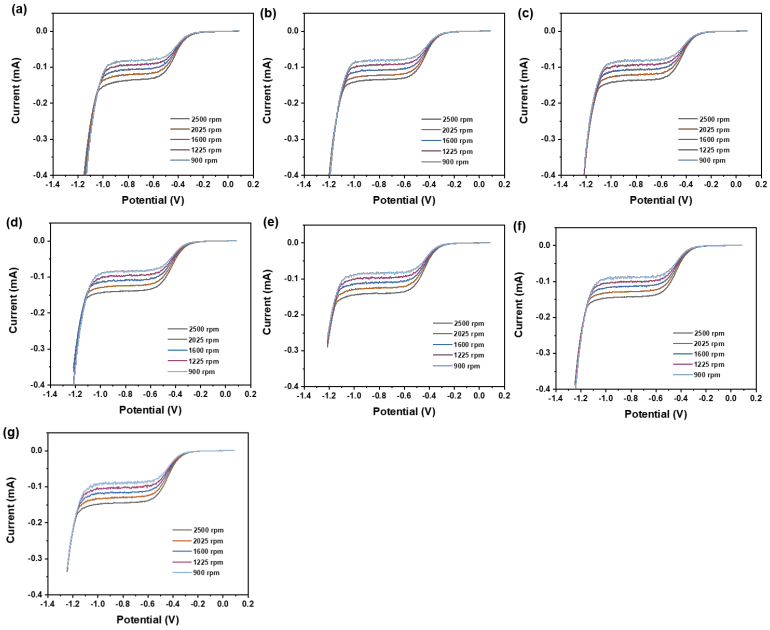

Figure S6. **a-g)** Polarization curves recorded on a Au RDE at 10 mV s^{-1} with rotation rates from 900 rpm to 2500 rpm at a bulk pH of 4 in Ar-saturated 0 mM, 5 mM, 15 mM, 30 mM, 45 mM, 60 mM, 75 mM Na_2SO_4 respectively, Li_2SO_4 was added to adjust the ionic strength.

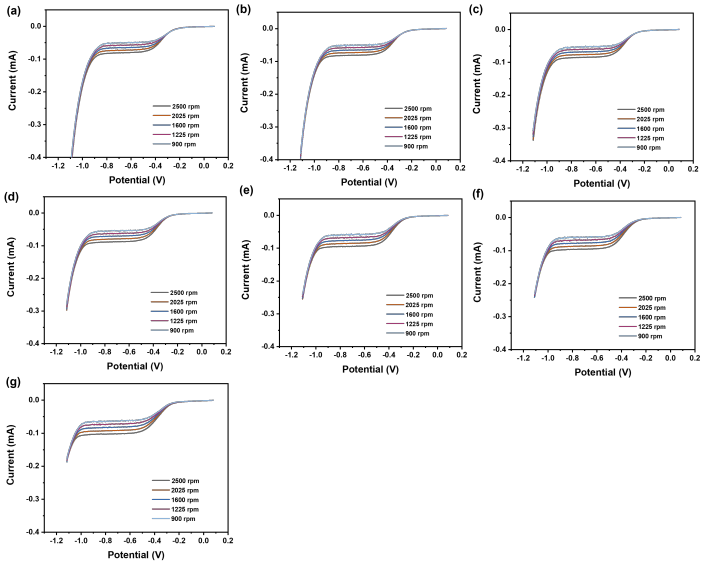

Figure S7. **a-g)** Polarization curves recorded on a Au RDE at 10 mV s^{-1} with rotation rates from 900 rpm to 2500 rpm at a bulk pH of 3.7 in Ar-saturated 0 mM, 5 mM, 15 mM, 30 mM, 45 mM, 60 mM, 75 mM $CsClO_4$ respectively, $LiClO_4$ was added to adjust the ionic strength.

The effect of Na^+ on the steady-state behavior of HER

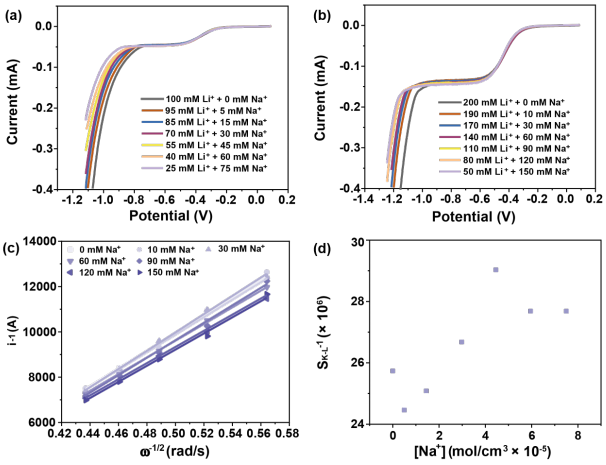

Figure S8. **a)** Polarization curves recorded on a Au RDE in Ar-saturated 100 mM sulfate electrolytes with different ratios of cation concentrations, with a bulk pH of 4, at 10 mV s^{-1} and a rotation rate of 2500 rpm. **b)** Polarization curves recorded on a Au RDE in Ar-saturated 100 mM perchlorate electrolytes with different ratios of cation concentrations, with a bulk pH of 4, at 10 mV s^{-1} and a rotation rate of 2500 rpm. **c)** Koutecký-Levich plots under different electrolyte conditions from a) with the rotation rates ranging from 900 rpm to 2500 rpm. **D)** The correspondence between the S_{K-L}^{-1} and the Na^+ concentration from b).

A quantitative analysis at bulk pH of 3.7

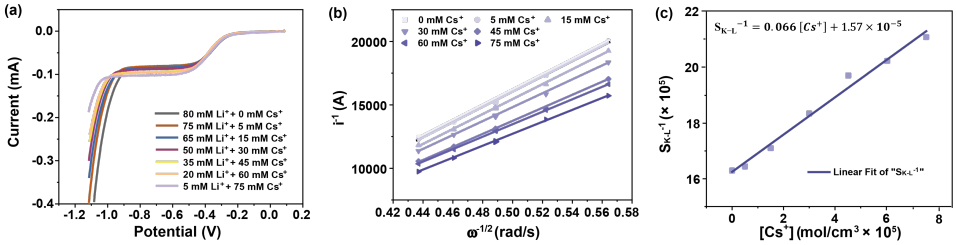

Figure S9. a) Polarization curves recorded on a Au RDE in Ar-saturated 100 mM perchlorate electrolytes with different ratios of cation concentrations, with a bulk pH of 3.7, at 10 mV s^{-1} and a rotation rate of 2500 rpm. **b)** Koutecký-Levich plots under different electrolyte conditions from a) with the rotation rates ranging from 900 rpm to 2500 rpm **c)** The correspondence between the $S_{K\text{-}L}^{-1}$ and the K^+ concentration from b) and its linear fit.

Reference

(1)Koutecky, J.; Levich, V., The use of a rotating disk electrode in the studies of electrochemical kinetics and electrolytic processes. *Zh. Fiz. Khim* **1958,** *32*, 1565-1575.

(2)Dogonadze, R., Use of Rotating Disk Electrode in the Study of the Electrochemical Kinetic and Catalytic Processes. The Case of Different Diffusion Coefficients. *Zh. Fiz. Khim.* **1958,** *32*, 2437-2442.

(3)Treimer, S.; Tang, A.; Johnson, D. C., A Consideration of the application of Koutecký-Levich plots in the diagnoses of charge-transfer mechanisms at rotated disk electrodes. *Electroanalysis* **2002,** *14* (3), 165-171.

(4)Leal, P.; Leite, N.; Viana, P.; de Sousa, F.; Barcia, O.; Mattos, O., Numerical analysis of the steady-state behavior of CE processes in rotating disk electrode systems. *Journal of The Electrochemical Society* **2018,** *165* (9), H466.

(5)Rebouillat, S.; Lyons, M. E. G.; Bannon, T., Evaluation of the proton transfer kinetics of potential electrolytes in non-aqueous solutions using electrochemical techniques Part 1. Kinetic analysis of the general CE mechanism at stationary and rotating electrodes. *J. Solid State Electrochem.* **1999,** *3* (4), 215-230.

(6)Lide, D. R., *CRC handbook of chemistry and physics*. CRC press: 2004; Vol. 85.